Multiscale tarsal adhesion kinematics of freely-walking dock beetles

Sophie Marie Gernay,[1,2] Simon Labousse,[1] Pierre Lambert,[2] Philippe Compère,[3] and Tristan Gilet[1,*]

[1] *Microfluidics Lab, Department of Aerospace and Mechanical Engineering, University of Liège, B-4000 Liège, Belgium*

[2] *TIPs, Université Libre de Bruxelles*

[3] *Laboratoire de Morphologie Fonctionnelle et Evolutive, University of Liège, B-4000 Liège, Belgium*

In this experimental study, living dock beetles are observed during their free upside-down walk on a smooth horizontal substrate. Their weight is balanced by the adhesion of hairy structures present on their tarsomeres. The motions involved in the attachment and detachment of these structures were characterised by simultaneously imaging the beetle from the side at the body scale, and from the top at the scale of a single tarsal chain. The observed multiscale three-dimensional kinematics of the tarsi is qualitatively described, then quantified by image processing and physically modelled. A strong asymmetry is systematically observed between attachment and detachment kinematics, both in terms of timing and directionality.

Keywords: Gastrophysa, capillary adhesion

1. INTRODUCTION

Many hexapod species have the ability to walk on a wide variety of surfaces. As a consequence, they have been incredibly successful at colonising terrestrial habitats. Some plants that are victim of phytophagous insects have developed slippery surfaces as a counterpart in the evolutionary arms race [1, 2]. Hexapod terrestrial locomotion and attachment have been investigated for more than 150 years [3]. Early experiments with freely walking beetles on various substrates revealed that the main contributors to adhesion were Van der Waals forces and capillary forces from the pad secretion [4].

Hexapod adhesion mechanisms are not only interesting for the development of reusable bio-inspired adhesives [5–8]. They also are a promising answer to a current challenge in microrobotics: with conventional prehension (tweezers, vacuum), it is hard to pick and place objects smaller than 100 μm without being impaired by Van der Waals forces [9, 10]. The reversible adhesion of hexapods does not seem to suffer from this size limit. Many hexapods possess tarsomeres (tarsal segments) covered with slender adhesive structures called tenent (adhesive) setae (hairs), of a diameter of the order of a few micrometers only.

In this work, the dock beetle *Gastrophysa viridula* De Geer (Coleoptera, Chrysomelidae) was used as a model species. The adhesion mechanism of this beetle has been the subject of many studies in the last fifteen years (e.g., [11]). Standardised rearing procedures have been reported, with the aim of ensuring that individuals are at the same development stage [12, 13]. The beetles possess five tarsal segments (tarsomeres t1-t5, proximal to distal, respectively). The distal segment t5 bears the claws. The fourth tarsomere t4 is hidden. Tarsomeres t1-t3 are ventrally covered with adhesive pads composed of tenent setae. We further call them proximal, middle and distal adhesive pad, respectively (figure 1). During locomotion, the setae not only have to adhere well on many different substrates but they must also detach quickly and effortlessly. Usually, only the tip of each seta touches the substrate. More exactly, the adhesion is mediated by some liquid on the seta tips; a part of it is left as footprints [14]. The composition of this liquid seems to be derived from cuticular lipids [15]. There are three main different shapes of seta tips: spatulate [16], discoidal and pointed [17]. They have different mechanical properties: discoidal tips are stiffer, and they provide significantly more adhesion than other tips [17, 18]. Discoidal tips are found only in males. They can provide strong attachment to the female elytra during copulation [17]. Dock beetles are very well adapted to locomotion onto their main source of food: dock leafs [19, 20].

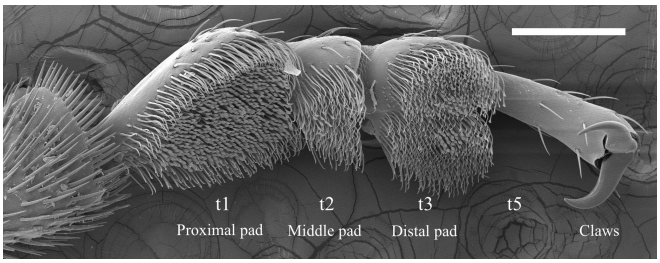

FIG. 1. Scanning Electron Microscope image of the ventral tarsus of a male dock beetle *Gastrophysa viridula*. The tarsus (foot) consists of 5 tarsomeres (t1-t5). The 5th tarsomere bears claws. Tarsomeres t1-t3 are ventrally covered with tenent setae, and further called proximal, middle and distal adhesive pads. The scale bar is 200 μm.

* Tristan.Gilet@ulg.ac.be

Adhesive structures have evolved independently mul-

tiple times within hexapods. The observed convergent evolution of many species towards this strategy of fibrillar adhesion (e.g. earwigs, beetles and flies) strongly suggests a function-driven evolution [21]. It therefore represents a relevant source of inspiration for microrobotic pick-and-place, which faces similar requirements in terms of speed and robustness to various substrates.

The excellent performance of walking hexapods is due to the fact that they move their elaborated adhesive pads with the appropriate kinematics at the scale of the leg. Mechanosensitive tarsal sensilla are often present on tarsomeres [22, 23]. By constrast, the muscles that activate the claws (through tendons) are located in the tibia [24], so there is no muscular control at the scale of individual setae. Beetles and flies do not usually have any antagonist muscle to the flexor muscle [24, 25]. As a consequence, they can only lift their claw by contracting this flexor muscle, or move the entire tarsus at once. While many studies were dedicated to quantifying the geometry and mechanical behaviour of the pads subjected to forced kinematics [17, 18, 26–29], the description of free-walk kinematics remained mostly qualitative [25, 26]. Moreover, only hypotheses could be made on the motions responsible for generating the required adhesion then cancelling it a fraction of second later.

A universal gait was observed for most adult hexapods, which consists in the cycle "HR-FL-MR-HL-FR-ML", where F, M and H correspond to front, mid- and hind legs, while L and R identify left and right legs, respectively [30, 31]. This gait reduces the net turning-moment of the body, so the hexapod can walk in a straight line [30]. The sequence seems independent of the inclination of the substrate on which the hexapod walks [32]. Only the overlap of stance phases is more important during upside-down walking [32], which should increase the total average adhesion force. Insects with a large safety factor (attachment force over body weight) can move three legs at a time – (FR, ML, HR) vs. (FL, MR, HL) – when upside-down, as in a classical tripod gait [33]. Others prefer a more continuous sequence, where maximum two legs swing at a time so the insect continuously benefits from the adhesion of at least four legs [30].

The detailed motion of the pulvilli (hairy adhesive pads at the base of the claw) of both flies *Calliphora vicina* Rob.-Des. and *Musca domestica* L. (Diptera, Calliphoridae and Muscidae, respectively) was observed with high speed microscopy imaging [25]. Flies were free to walk inside a tube, whose orientation was varied. These observations revealed a systematic proximad movement of the tarsomeres at the beginning of the stance phase. Also, four detachment scenarios were observed (with percentage of occurrence in brackets, for 129 events):

1. Twisting (40%): The leg is rotated by up to 90^o in the plane parallel to the substrate, before it is pulled proximally.

2. Lifting (27%): The leg is lifted from the proximal side, which causes the claw to be passively pressed to the substrate. The setae are then progressively peeled in the distad direction.

3. Pulling (24%): The leg is pulled proximally until it detaches. This motion probably requires a larger force, and it possibly happens only when the fly is stressed. The proximal pad detaches first.

4. Shifting (9%): The leg is briefly pushed distally, which compresses the pulvilli. The median pad detaches first.

Unfortunately, this first investigation of fly tarsomere kinematics [25] did not include any quantification of the motion, and scale bars were not reported. Moreover, among hexapods the pulvilli are specific to a limited number of species, including flies (Diptera) and some true bugs (Heteroptera, e.g. Pentatomidae, Miridae, Thaumastocoridae) [34]. So it is unclear if the corresponding kinematics is shared by other hexapods without pulvilli.

The ventral pads on the first to third tarsomere of dock beetles seem to serve different functions, as it was shown for males freely walking up and down on a smooth vertical surface [26]. Previous studies showed that, on the one hand, the distal pad experiences stronger and longer contact than others when adhesion is required (e.g., on forelegs when climbing up, or on hindlegs when climbing down). It is the first to attach and the last to detach. On the other hand, the proximal pad is fully used when the legs are in compression (e.g., forelegs when climbing down). Measurements of the force resulting from the compression of the pads (displacement of about 20μm towards the substrate) revealed that proximal pads are significantly stiffer than distal pads, which would help them to avoid buckling [26].

The forces experienced by the pads are also strongly dependent on their direction of motion [14, 26]. Experiments with constrained living dock beetles showed that pads forced to slide over 10 mm at a speed of 500 μm s^{-1} generate significantly more shear force when pulled in the proximad direction than when pushed in the distad direction [14]. However, such distance and speed are far from the usual motions experienced by the pads of freely walking dock beetles. A similar force asymmetry between pulling and pushing was observed for cockroaches [35] and spiders [36].

The extent to which the walk kinematics of hexapods is controlled by neuronal feedback is still largely unknown [37]. Neuronal feedback was observed at the timescale of 200 ms for male cockroaches *Blaberus discoidalis L.* running on a substrate of roughness similar to their body scale [38]. The measured interburst interval was about 100 ms, which suggests that any motion at a smaller timescale cannot be attributed to neuronal control. Sponberg and Full [38] concluded that mechanical feedback plays a dominant role in self-stabilizing the insect locomotion. It could originate from the intrinsic viscoelasticity of the musculoskeletal structures.

This work aims at providing a detailed and quantitative kinematic study of the terrestrial locomotion of

dock beetles *G. viridula*. The beetles are freely walking upside-down on a horizontal, flat smooth surface. Synchronised views of the beetle motion are captured, each focusing on a different length scale, from the leg down to the individual setae. Each motion is quantified by image processing: the gait and leg kinematics, the peeling of the pads, the motion of the claws, and the peeling of individual setae. Our discussion of these motions will be guided by the hypothesis that every motion at a timescale less than 100 ms cannot be controlled in real-time by neuronal feedback, so that it should result from passive mechanical considerations only. Data from different views are correlated in order to identify motions occurring in concert. Our findings are regularly compared to previous work, especially on flies [25] in order to identify convergent features between flies and beetles. The appearance of such features in two species that have evolved independently would then suggest that these features are well-adapted to a given function, here terrestrial locomotion and attachment. Results are finally discussed with the aim of providing relevant advice to the design of future biomimetic devices based on hairy capillary adhesion.

2. EXPERIMENTAL SETUP

We studied 20 males of the dock beetle *Gastrophysa viridula* from our laboratory colony. Rearing was performed along the procedure described in Voigt *et al.* [12]. The temperature was kept between 20^{o}C and 25^{o}C, and the colony was subjected to daylight. Only adults of approximately the same age were selected for the experiments. Males were chosen because they possess the three different shapes of seta tips (spatulate, discoidal and pointed) thanks to which they adhere remarkably well on smooth surfaces [20]. The individuals were not distinguished. So in the subsequent statistical analysis, no distinction is made between repeated experiments on a single individual and experiments on distinct individuals. Significant statistical correlations observed while pooling all experiments would potentially be even stronger if a distinction of individuals was made.

The beetles were observed walking upside down from two points of views. A macroscopic side view of the walking beetle was captured at 60 frames per second with a Nikon 1 V3 camera, a macro lens (AF-S DX Micro Nikkor 85mm) and backlighting. The numerical resolution, evaluated on each movie, is of the order of 8 μm per pixel. Simultaneously, one leg was imaged from the top with a high speed camera (Phantom Miro 110) at 1600 frames per second, through a transmission microscope (Zeiss Axio Scope A1) with a 10x objective. The numerical resolution is 1.22 μm per pixel. In order to synchronise both recordings, the output signal of the high speed camera (top view) triggered the external light source of the side view. During each experiment, the beetle was first deposited, head up, at the center of a clean microscope slide (soda-lime glass, ISO 8037/1, Carl Roth). It was then gently turned upside down and placed in the field of view. The beetle was then free to walk. In order to keep it walking in the vertical focal plane of the side view, the lateral parts of the glass slide were covered with a superhydrophobic coating (Tegotop®210, Evonik Industries, and Antispread E2/200, Dr. Tillwich GmbH) which strongly limited adhesion and discouraged exploration outside the focal plane. To apply this coating locally, the central part of the glass slide was first masked with a slightly adhesive tape that did not leave any apparent glue residue once removed.

3. RESULTS AND DISCUSSION

A. Gait and leg kinematics in vertical planes

Our kinematic investigation started at the scale of the beetle, i.e. a few millimetres. The beetle was observed in a vertical plane from the side. We define the cartesian coordinate system (x, y, z) oriented along the beetle body, where x is the horizontal longitudinal axis (from posterior to anterior, i.e. increasing during a motion forward), y is the horizontal lateral axis (from its right to its left), and z is the vertical axis (perpendicular to the substrate, from ventral to dorsal, i.e. downwards here).

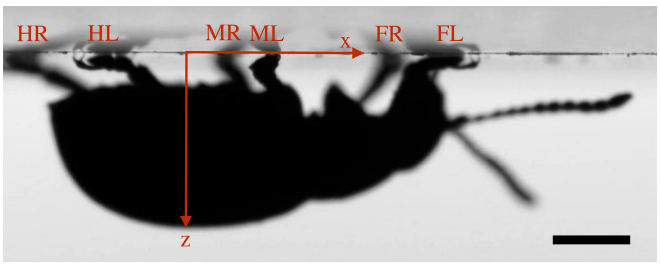

FIG. 2. Macroscopic side view (x, z) of a male dock beetle walking upside down a glass substrate. Legs are numbered with two letters: the first differentiates forelegs (F), midlegs (M) and hindlegs (H); the second indicates left (L) or right (R). Left legs are here in focus, while right legs are out of focus. The scale bar is 1 mm. The corresponding movie is available in the Supplementary Material.

In some videos of interest, the beetle walked at approximately constant speed in the direction perpendicular to the camera (sagittal view). Each leg could then be distinguished and identified (figure 2) in the (x, z)-plane: e.g. left legs stayed in focus while right legs were out of focus. The gait could then be properly analysed (figure 3).

We first measured the swing duration t_{sw} (when the leg is separated from the substrate), as well as the contact position x of each leg during the stance phase (figure 3a). Left and right legs moved alternately. At $t = 0.8$ s, the gait converged to a regular sequence HR & FL, MR, HL & FR, ML already described by Hughes [30]. Each front leg swung at approximately the same time as the opposite

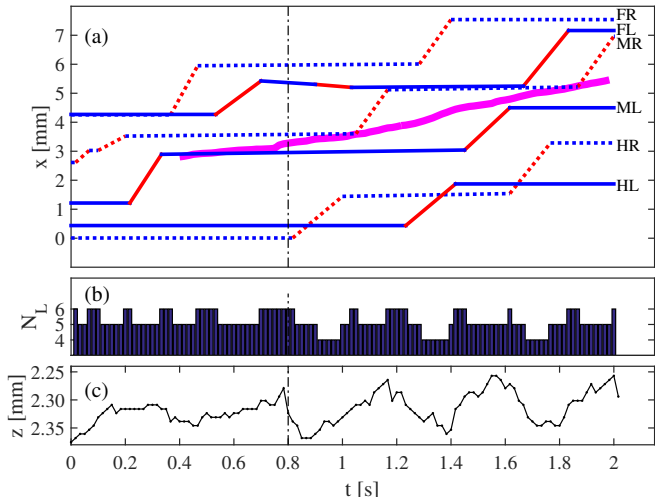

FIG. 3. Gait pattern. The dash-dot vertical line indicates the beginning of the regular gait. (a) The position x of each leg is represented as a function of time (solid lines for left legs, dotted lines for right legs). Blue (resp. red) lines correspond to the stance (resp. swing) phase. The thick magenta line is the central position of the body. (b) Number of legs N_L in contact with the substrate (stance phase). (c) Vertical distance z, oriented downwards, from the substrate to the lowest point of the elytra.

hind leg. This is confirmed by the bar plot in figure 3b that represents the number of legs N_L in stance at a given time. It oscillated between 4 and 6 so the insect swung maximum two legs at a time. Steps were not regular, they varied in both duration and distance, but they were all of the same order of magnitude. The swing duration is $t_{\rm sw} \simeq 0.13$ s, which is about 1/6th of the gait sequence (cycle frequency 1.3 Hz). It is also the same order of magnitude as the neuronal response time measured for cockroaches [38]. The legs moved forward by $\Delta x \simeq 1.5$ mm at each step on average, so the mean speed of each leg was about $\Delta x/t_{\rm sw} \sim 12$ mm s^{-1}. The dimensionless Froude number Fr is used in terrestrial locomotion analysis as the ratio between inertial forces (e.g. centripetal) resulting from leg motion and the weight of the animal. It is defined as $Fr = L/(gt_{\rm sw}^2)$, where L is the leg length and g is the gravity acceleration. The transition from walking-like gaits to running-like gaits typically occurs when $Fr \sim 1$ [39]. Since $L \sim 2$ mm, $Fr \sim 0.01 \ll 1$. Therefore, the gait was clearly in a walking-like regime: inertial forces resulting from leg motion were negligible in comparison to the leg weight. Consequently, the weight of the beetle and the reaction forces from the substrate had to almost balance at all time.

We also measured the displacement of the upper line of the closed beetle elytra which, in first approximation, is the same as the motion of the centre of mass of the beetle. The average horizontal walking speed on ceiling is approximately 1.7 mm s^{-1} (figure 3), which is indeed about 1/6th of the average leg speed. When the gait was stabilised ($t > 0.8$ s) the beetle body moved cyclically up and down with amplitude and frequency of about 100 μm and 2.5 Hz respectively (figure 3c). This corresponds to twice the cycle frequency. The body was the lowest when two legs swung at a time.

The swing time $t_{\rm sw}$ and corresponding advance of the leg Δx in the x-direction were recorded more systematically on side views (x, z), for 176 leg swings – not all of them during stabilised walking (Data available in the Supplementary Material). The swing time is $t_{\rm sw} = 0.15_{[0.13,0.18]}$ s, where 0.15 denotes the median value, and the numbers in bracket correspond to the first and third quartiles (this notation is used throughout this paper). It is twice as much as the swing time of the blow fly *C. vicina* [25], though this latter was observed walking right-side-up on a horizontal substrate. The corresponding travelled distance is $\Delta x = 0.54_{[0.37,0.91]}$ mm and the leg speed is $4.2_{[2.2,6.4]}$ mm s^{-1}, which is three times smaller than for the sustained gait of figure 3. The variability from one step to another is much larger in terms of distance travelled Δx than in terms of swing time. The maximum observed distance $\Delta x \simeq 2$ mm is of the order of the leg length. No pronounced differentiation between fore-, mid- and hind-legs is observed (ANOVA $F_{2,172} = 1.81$, $p = 0.17$).

When bored of being in the limelight, the beetle had the ability to detach its 6 legs in less than 17 ms, and to fall (figure 4). Right after detachment, most of the claws were still in contact with the substrate, which suggests that they were here used as the fulcrum of a lever to initiate detachment.

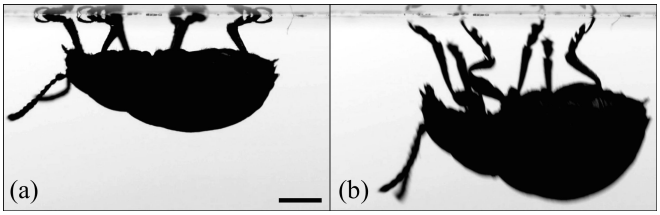

FIG. 4. Macroscopic side view of a male dock beetle. (a) The beetle is firmly attached with its 6 legs in contact with the substrate. (b) 17 ms after, all six legs detached from the substrate and the beetle was then in free fall. The scale bar is 1 mm.

The rotation of the leg is better seen in the (y, z)-plane, i.e. when the posterior-anterior axis of the beetle $\mathbf{e}_x$ was parallel to the axis of the camera (transverse view). An example of swing kinematics of the left hindleg (HL) is shown in Figure 5. It is a non-trivial combination of translation and rotation, which is often asymmetric in time: here, the motion away from the substrate was about twice slower than the subsequent motion towards the substrate. A similar observation was made for blow flies *C. vicina* [25]. Their swing phase ended with a slight pull of the leg in the proximad direction

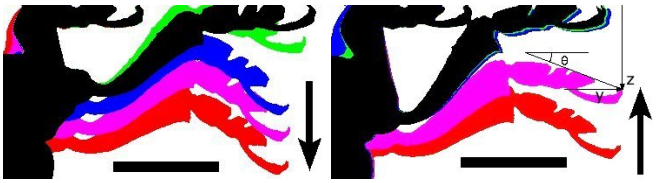

(a) (b)

FIG. 5. (a) Detachment and (b) attachment kinematics of the left hindleg in the (y, z)-plane (seen from behind the beetle). The colour sequence [black, green, blue, magenta, red], reversed in (b), represents successive positions every 17ms. The large notched arrow indicates the direction of leg motion. The scale bar is 1 mm.

once the substrate had been touched. The claw position $[y(t), z(t)]$ and leg orientation $\theta(t)$ were tracked on six similar movies (Data available in the Supplementary Material). The maximum vertical distance from the slide to the claw $z_M = \max(z) = 1.1_{[0.7,1.9]}$ mm varies significantly from one step to another. The horizontal speed $\dot{y} = 4.2_{[1.4,5.5]}$ mm s^{-1} is one order of magnitude lower than the maximum vertical speed $|\dot{z}_M| = 28_{[10,140]}$ mm s^{-1}. The average vertical acceleration is $\ddot{z} \simeq -0.64$m s^{-2}. The swing time can be approximated as $t_{\rm sw} \sim 4z_M/\dot{z}_M = 0.12_{[0.11,0.13]}$ s, consistently with other estimations here above.

B. Pad sequence

We also analysed the sequence in which the three pads (distal, middle and proximal) of a leg get attached to and detached from the substrate. For attachment (resp. detachment), we define t_D as the first (resp. the last) time at which at least 15μm^2 of the distal pad were attached. Times t_M and t_P are defined similarly for the middle and proximal pads. The difference between these times t_D, t_M and t_P is represented in Figure 6. On the one hand, several different attachment sequences were observed: either pad can be first to attach, as long as the middle pad is not the last. This is in contrast to previous reports that the distal pad should always be first to attach [26]. On the other hand, detachment is more selective: the most likely sequence is by far P-M-D, so the proximal pad detaches first, then the middle pad then the distal pad (as observed in [26]). Only in one occurrence could the middle pad detach much before the other two.

C. Area of contact

High-speed microscopy imaging provide a wealth of quantitative information on the horizontal motion of the legs (top, frontal view - figure 7). We recorded and processed videos of 17 attachment and 23 detachment events. In order to describe the corresponding kinematics quantitatively, we define local coordinates (X, Y) based on the

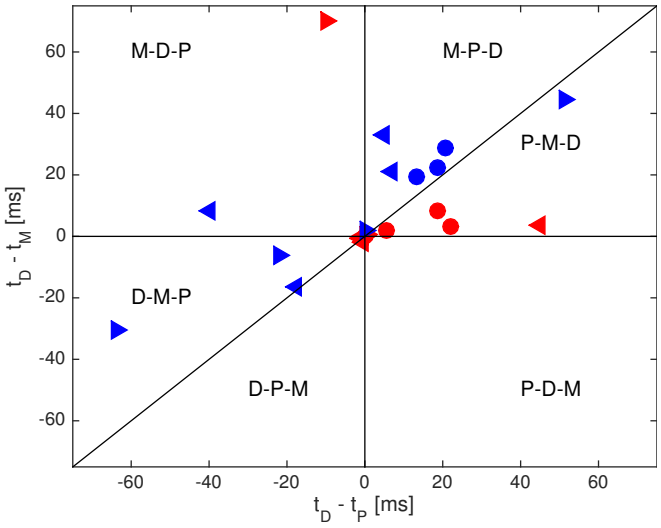

FIG. 6. Plot of the pad sequence, represented by the difference between the time of attachment (resp. detachment) of each pad: t_D for the distal pad D, t_M for the middle pad M, and t_P for the proximal pad P. Blue (resp. red) symbols correspond to attachment (resp. detachment). Symbol shapes indicate tarsomeres of which leg are considered: ◁ = foreleg, • = midleg, ▷ = hind-leg. For example, the symbol ◀ on the right side of zone P-M-D means that in the corresponding experiment on a foreleg, the proximal pad detached first, then the middle and finally the distal. The proximity to the x-axis indicates that the distal pad detached a few milliseconds after the middle pad.

stance position of the leg (Figs. 7–8). The Y-axis $\mathbf{e}_Y$ is oriented along the symmetry axis of the claw, from proximal to distal. The X-axis $\mathbf{e}_X$ is oriented at 90^o from $\mathbf{e}_Y$, clockwise in microscope pictures, so $\mathbf{e}_X = \mathbf{e}_Z \times \mathbf{e}_Y$. For any vector $\mathbf{b}$, we define the directional cosines:

$$\Psi_X(\mathbf{b}) = \frac{\mathbf{b}\cdot\mathbf{e}_X}{|\mathbf{b}|}, \quad \Psi_Y(\mathbf{b}) = \frac{\mathbf{b}\cdot\mathbf{e}_Y}{|\mathbf{b}|} \qquad (1)$$

During the stance phase, individual seta tips did usually experience sufficient adhesion to instantly stop moving as soon as they touched the substrate. Nevertheless, in 32% of the cases they slid over a distance comparable to the pad size before they fully adhered to the substrate. This sliding is revealed in red through image superposition, as illustrated in figure 9. When sliding was considered absent, setae were not seen to move significantly before the preparation of the next detachment.

We first measured the maximum number of seta tips $N_c \simeq 263_{[228,355]}$ in contact for each leg, and the corresponding contact area $S_c \simeq 5400_{[3700,8400]}$ μm^2 during the stance phase (figure 7-left – Data available in the Supplementary Material). The portion of contact is on average distributed in the proximal pad (21%), the middle pad (12%) and the distal pad (66%). The adhesion force that individual spatula-shaped seta tips can generate is estimated to be 0.6 μN [17], so the total force that

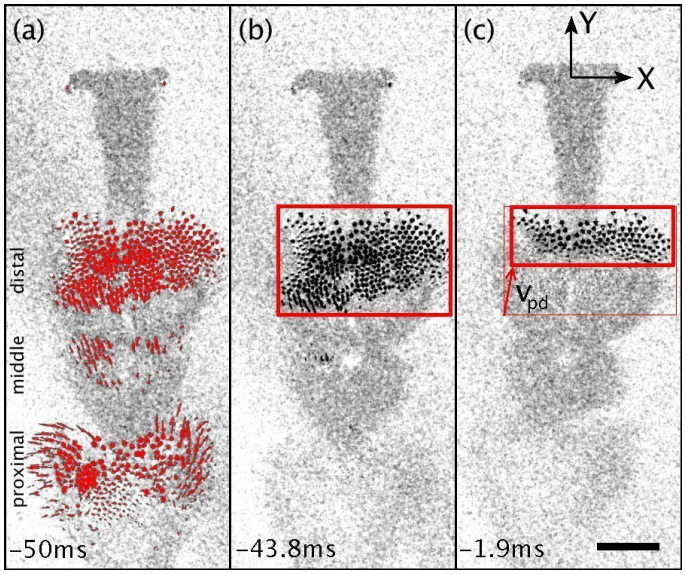

FIG. 7. Detachment of a ventral FR tarsus (top view). Time is indicated with respect to the time at which the last seta detaches. Both the scale bar and the (X, Y) axes are 100 μm long. (a) Stance phase: setae in contact with the substrate are highlighted in red (number of distinct seta tips N_c, surface area of these tips S_c). (b - c) The bounding box surrounds setae in contact for the distal pad. The associated velocity is $\mathbf{v}_{\rm pd}$.

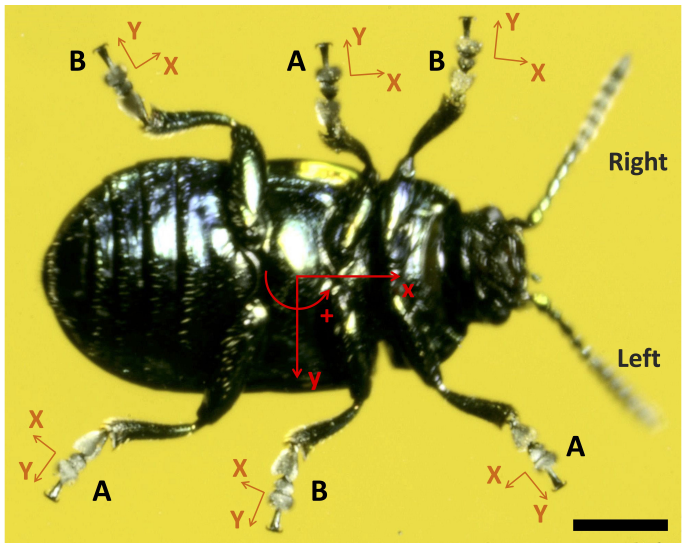

FIG. 8. Sign convention. Body coordinates (x, y) and leg coordinates (X, Y). Each leg belongs to one tripod (A) or (B). The scale bar is 1 mm. In the subsequent analysis, rotations of the claws around a vertical axis are considered positive when seen counterclockwise in the microscope top view (red arrow).

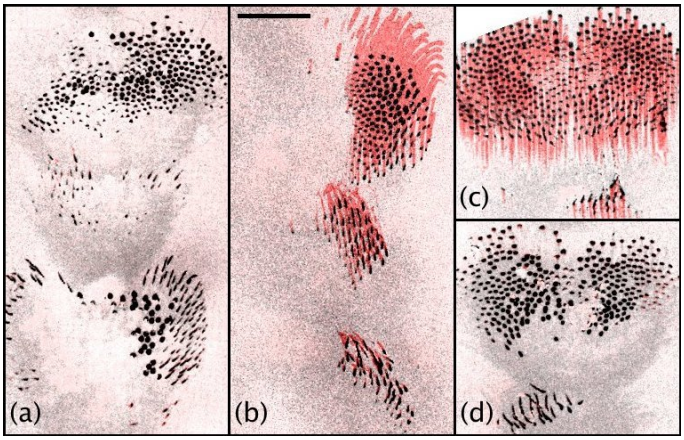

FIG. 9. Presence or absence of sliding (top view of ventral tarsi). For attachment (resp. detachment), the final (resp. initial) position of the setae appears in black. The red lines correspond to setae sliding during contact with the substrate. The scale bar is 100 μm. (a) Attachment without sliding (for at least 0.4 s) of a ML tarsus. (b) Attachment with proximad sliding (in 0.44 s) of a HR tarsus. (c) Detachment with proximad sliding (in 22 ms) of a FL tarsus. (d) Detachment without sliding (for at least 20 ms) of a ML tarsus.

could be generated is of the order of 158 μN for each leg and almost 1 mN for the six legs in full contact. This force outbalances the weight of the insect (10.8 mg for the average male dock beetle [26]) by a factor of nine. It could even be larger, as 6 legs in simultaneous contact would yield more adhesion than six times the adhesion of one single leg in contact. This fact was observed for spiders, which also rely on hairy pads for adhesion [28]. In any case, inertial forces, which should be considered in addition to the weight, are here negligible since $Fr \ll 1$.

We also tracked the time evolution of the contact area $S(t)$, during both attachment and detachment. We define the attachment time $t_{\rm a}$ (resp. detachment time $t_{\rm d}$) as 3/2 of the minimum time that it took for $S(t)$ to increase (resp. decrease) by 2/3 of $S_{\rm c}$, all pads being considered together (figure 10). Quartiles are reported in Table I, and the influence of sliding is assessed through a two-sample t-test. The attachment time is approximately $t_{\rm a} \sim 150$ ms. The influence of sliding seems negligible ($p = 0.7$), but the test has a very low statistical power (0.07), owing to the small number of samples. By contrast, the detachment time is one order of magnitude smaller, and it strongly increases with sliding, with statistical significance ($p = 0.05$, power 0.84).

For the distal pad, we also recorded the increase (resp. decrease) of the bounding box surrounding the seta tips in contact during attachment (resp. detachment), as illustrated in figure 7(middle and right). We then define the peeling velocity $\mathbf{v}_{\rm pa}$ (resp. $\mathbf{v}_{\rm pd}$) as the average of the velocity of each side of the box (left, right, proximad and distad), each being counted positive if in the $\mathbf{e}_X$ or $\mathbf{e}_Y$ direction: $\mathbf{v}_{\rm pa/d} = (V_{left} + V_{right})\mathbf{e}_X + (V_{proximad} +$

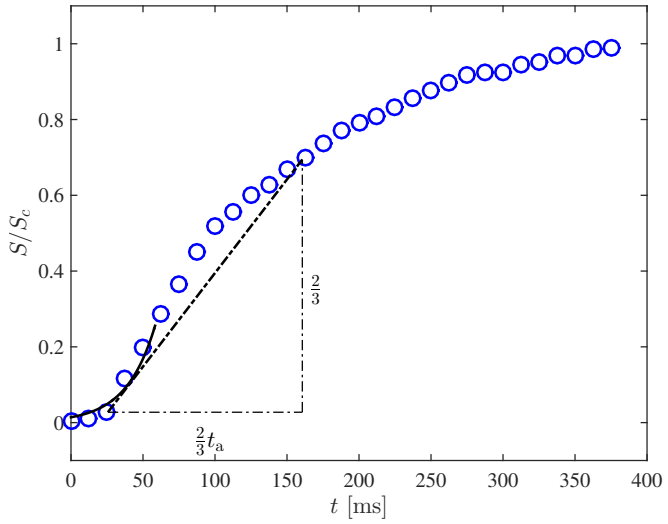

FIG. 10. Surface area $S(t)$ of the seta tips in contact with the substrate during attachment of a mid-leg, normalised by the surface area S_c at the end of attachment (maximal area during the stance phase). The dash-dot lines represent the increase of 2/3 in a time $2/3t_a$. The solid line corresponds to the early-time approximation by the exponential growth of Eq.(5).

TABLE I. Attachment time t_a (resp. detachment time t_d) of the tarsal segments and corresponding peeling speed $\mathbf{v}_{pa}$ (resp. $\mathbf{v}_{pd}$), quantified by its magnitude and its directional cosine Ψ_Y. The main numbers correspond to median values, while the numbers in brackets represent the first and third quartiles. The p-value corresponds to a two-sample t-test on the influence of sliding. The corresponding statistical power is given in the last column (for a significance level of 0.05). Data are available in the Supplementary Material.

	Static	Sliding	t-test	
Sample #	13	4	p	power
t_a [ms]	$150_{[100,210]}$	$97_{[86,190]}$	0.70	0.07
$\lvert\mathbf{v}_{pa}\rvert$ [mm s^{-1}]	$1.1_{[0.7,3.8]}$	$5.4_{[2.7,7.2]}$	0.96	0.05
$\Psi_Y(\mathbf{v}_{pa})$	$-0.6_{[-0.9,0.1]}$	$0.1_{[-0.7,0.8]}$	0.34	0.17
Sample	14	9	p	power
t_d [ms]	$7.5_{[4.7,14]}$	$23_{[8.4,60]}$	0.05	0.84
$\lvert\mathbf{v}_{pd}\rvert$ [mm s^{-1}]	$29_{[9.4,60]}$	$34_{[11,68]}$	1.00	0.05
$\Psi_Y(\mathbf{v}_{pd})$	$0.8_{[0,1]}$	$-0.1_{[-0.6,0.7]}$	0.17	0.28

V_{distad})$\mathbf{e}_Y$. As seen in Table I, the magnitude of the peeling speed is one order of magnitude larger during detachment than during attachment. In the static case (without sliding), the average peeling speed multiplied by the attachment/detachment time always yields a peeling distance of the order of 200μm, which approximately corresponds to the length of the distal pad. This length gets increased by the sliding distance, of the order of 300 to 600 μm. The peeling direction is more often proximad during attachment ($\Psi_Y(\mathbf{v}_{pa}) < 0$) and distad during detachment ($\Psi_Y(\mathbf{v}_{pd}) > 0$). This latter observation is consistent with the dominant pad sequence P-M-D of detachment. Sliding does not seem to influence the peeling speed (although the power of the test is again weak), but it does make directionality less systematic ($\Psi_Y(\mathbf{v}_{pa/d}) \sim 0$ on average).

D. Claw motion in the horizontal plane

The claw remained entirely in the field of view in 7 attachment and 7 detachment high-speed movies. The kinematics of this solid body can be described by the motion of the segment joining both claw tips. The segment is characterised by the position of its mid-point $\mathbf{R}(t)$ and by its orientation $\phi(t)$, counted positive if counterclockwise in microscope pictures. Only the rotation of the claw in the (x, y) horizontal plane could be properly analysed. The side view does not allow for a systematic quantification of rotations in a vertical plane. The origin of time $t = 0$ corresponds to when the first seta attaches to (resp. the last seta detaches from) the substrate. The position $\mathbf{R}$ is set to zero (origin of the axes $\mathbf{e}_X$ and $\mathbf{e}_Y$) at that time.

1. *Attachment*

A typical attachment sequence is shown in figure 11, and the corresponding evolution of $\mathbf{R}$ is represented in figure 12. As seen from the claws, the leg strongly decelerated as soon as the very first setae made contact with the substrate ($t = 0$). Then ($t > 0$), the leg was pulled in the proximad direction over a few tens of micrometers and the claw position $\mathbf{R}$ converged to $\mathbf{R}_a$. This pulling after contact has already been observed for dock beetles [14], and very similarly for blow flies (*C. vicina*) [25] and geckos [40]. Pulling on the tarsomeres could help bringing individual seta tips into intimate contact with the substrate, and it could then introduce a shear load on the setae [33].

We identified the claw motion on 7 attachment movies (table II). Right before attachment ($t \to 0^-$), we approximated the motion by:

$$\mathbf{R}(t) = \dot{\mathbf{R}}_{0a} t \quad \phi(t) = \dot{\phi}_{0a} t + \phi_{0a}. \tag{2}$$

The horizontal claw speed at approach $|\dot{\mathbf{R}}_{0a}|$ is around 15 mm s^{-1} without significant influence of sliding. The approach direction is slightly proximad ($\Psi_Y(\dot{\mathbf{R}}_{0a}) < 0$), especially when sliding is observed. The corresponding angular speed $|\dot{\phi}_{0a}|$ is about 19 rad s^{-1}, and it is less when sliding is present. This approach kinematics, if approximately maintained during half of the swing ($t_{sw}/2$), would correspond to an average travelled distance of 0.7 mm and an average rotation angle of 70^o (without sliding), which are both consistent with our measurements from the side view.

The first few setae that touched the substrate generated a strong deceleration of the leg, both parallel and

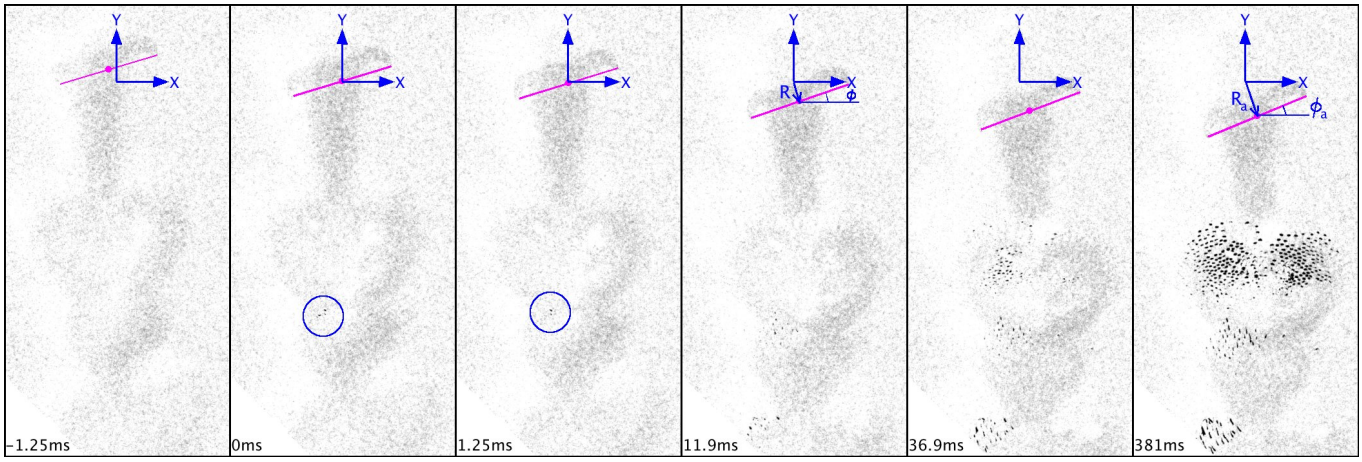

FIG. 11. Top view of the attachment of the ventral tarsus of a male left mid-leg. The time of each frame is indicated in the lower left corner; time $t = 0$ corresponds to the first setae touching the substrate (circled in blue). Axes (X, Y) are of length 100 μm, and centred on the position of the claw at time $t = 0$. The position and orientation of the claw are measured with $\mathbf{R}(t)$ and $\phi(t)$ respectively. The final position (resp. orientation) is $\mathbf{R}_\mathrm{a}$ (resp. ϕ_a). The corresponding movie is available in the Supplementary Material.

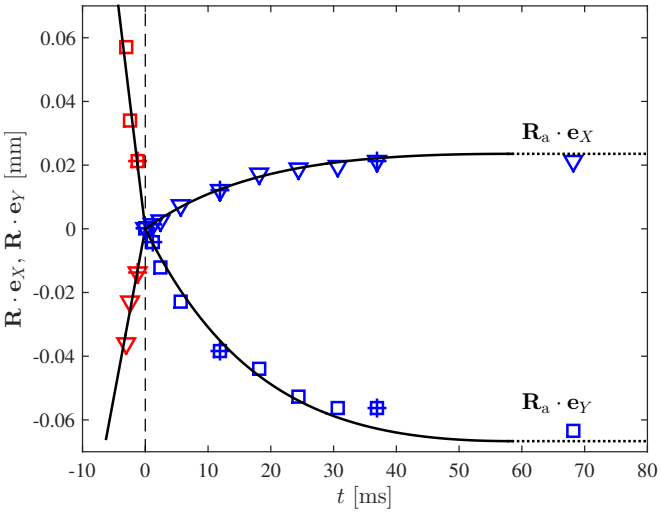

FIG. 12. Claw kinematics during attachment: Approach (red) and proximad pull right after touching (blue). Triangles ($\triangledown$) represent $\mathbf{R}(t) \cdot \mathbf{e}_X$ while squares ($\square$) represent $\mathbf{R}(t) \cdot \mathbf{e}_Y$.The crossed symbols correspond to the snapshots of figure 11. The thick lines correspond to Equations(2) and (6). The horizontal dotted lines indicate the magnitude of the X and Y components of $\mathbf{R}_\mathrm{a}$. The vertical dashed line is $t = 0$.

normal to the substrate. In Figure 11, the deceleration was not mediated by the impact of the claw. Indeed, claw tips were not in focus so the claw did not touch the substrate yet (by opposition to the claw in figure 7). Would these first few setae crush under the impact of the leg on the substrate? The spring constant of the seta stalk was measured to be about 0.3 N m^{-1} for each spatula-shaped tips [17], which corresponds to 0.6 N m^{-1} for the two setae in contact at $t = 0$. The mass of the tarsal segments is estimated to $m \sim 4 \times 10^{-8}$kg (equivalent of a box of $1 \times 0.2 \times 0.2$ mm^3 with a density of 1 g/cm^3). If this mass compresses these two first setae, it behaves as a mass-spring system of natural frequency $\omega \simeq \sqrt{0.6/4 \times 10^{-8}} \sim 4 \times 10^3$ rad s^{-1}. If the leg initially approaches the substrate at a normal speed $|\dot{z}_M| \simeq 28$ mm s^{-1}, the setae are then pressed on the substrate by a distance of the order of $|\dot{z}_M|/\omega \sim 5\mu$m. This value is one order of magnitude smaller than the seta length, so the setae should bend without being crushed.

After initial contact ($t > 0$), the motion of the claw should be driven by a muscular force $\mathbf{F}_\mathrm{a}$ from the leg, which could only experience significant variations at the timescale of a few hundred milliseconds (i.e. the neuronal response time, or equivalently the swing time). The progressive slow-down of the claw suggests that the muscular force is opposed by an increasing friction force from the setae. It is here assumed proportional to the contact area $S(t)$. The proportionality factor, i.e. the shear stress $\sigma(t)$, is empirically modelled as

$$\sigma(t) = \sigma_0 + \alpha|\dot{\mathbf{R}}(t)| \qquad (3)$$

where σ_0 and α are constants, and it is assumed collinear with $\dot{\mathbf{R}}(t)$ at all time. Many phenomena could participate to this shear stress, including a solid/solid friction force, a lubrication force in the thin layer and wedge of liquid, a surface tension force from contact lines [18], or even some non-newtonian rheology. Their determination and modelling is left to future work.

The deceleration seen in figure 12 is of the order of 60 μm in 40 ms, so 37 mm s^{-2}. It corresponds to an inertial force on the tarsal mass m of the order of 1.5 nN, which is two orders of magnitude below the adhesion force exerted by one single seta. Consequently, inertial

forces can again be safely neglected and the force balance yields:

$$|\mathbf{F}_\mathrm{a}| = S(t)\left[\sigma_0 + \alpha|\dot{\mathbf{R}}(t)|\right] \quad (4)$$

As soon as $S(t)$ reaches $S_\mathrm{a} = |\mathbf{F}_\mathrm{a}|/\sigma_0$, the claw stops ($|\dot{\mathbf{R}}(t)| = 0$).

The full claw deceleration occurs at a timescale (60 ms in figure 12) significantly smaller than the attachment time t_a. Consequently, only the early part of the curve $S(t)$ in figure 10 has to be taken into account for Eq. (4). It can be approximated by an increasing exponential:

$$S(t) \simeq S_\mathrm{a} e^{\eta(t/\tau_\mathrm{a}-1)} \quad (5)$$

where τ_a is the characteristic time of claw deceleration and $\eta = \ln[S_\mathrm{a}/S(0)]$ is a dimensionless factor that corresponds to the amplification of contact area between $t = 0$ and $t = \tau_a$. The time evolution of $\mathbf{R}(t)$ is obtained by combining Eqs.(4-5) and integrating over time:

$$\begin{aligned}|\mathbf{R}(t)| &= \frac{\sigma_0\tau_\mathrm{a}}{\alpha}\left[\frac{e^\eta - e^{\eta(t/\tau_\mathrm{a}-1)}}{\eta} - \frac{t}{\tau_\mathrm{a}}\right] \\ &= |\mathbf{R}_\mathrm{a}|\frac{e^\eta - e^{\eta(1-t/\tau_\mathrm{a})} - \eta t/\tau_\mathrm{a}}{e^\eta - 1 - \eta} \end{aligned} \quad (6)$$

where

$$|\mathbf{R}_\mathrm{a}| = |\mathbf{R}(\tau_\mathrm{a})| = \frac{\sigma_0\tau_\mathrm{a}}{\alpha}\frac{e^\eta - 1 - \eta}{\eta} \quad (7)$$

is the distance over which the claw slides during attachment ($t > 0$).

Parameters $|\mathbf{R}_\mathrm{a}|$, τ_a, η and S_a are obtained by fitting simultaneously equations (5) and (6) on experimental curves $S(t)$ and $\mathbf{R}(t)$ of the 7 attachment movies (Figs. 10 and 12). The obtained quartiles are given in table II. The claw motion during attachment is always proximad ($\Psi_Y(\mathbf{R}_\mathrm{a}) < 0$), so the dock beetle pulls on its leg. The pulling timescale τ_a and length scale $|\mathbf{R}_\mathrm{a}|$ are about 36 ms and 58 μm, respectively. The dimensionless factor $\eta \simeq 2.6$ is almost constant in all experiments. The minimum contact area S_a necessary to stop the claw is 1.8×10^{-3} mm^2, which is about 33% of the average area at maximum contact S_c. The initial surface area $S(0)$ is then approximately $S_\mathrm{a}e^{-\eta} \sim 133$ $(\mu\mathrm{m})^2$, which corresponds to about 6 setae. The initial pulling speed

$$\left.\frac{d|\mathbf{R}|}{dt}\right]_{t=0} = \frac{|\mathbf{R}_\mathrm{a}|}{\tau_\mathrm{a}}\frac{\eta(e^\eta - 1)}{e^\eta - 1 - \eta} \simeq 5.3\mathrm{mm\ s^{-1}}$$

(without sliding) is significantly smaller than the approach speed $|\dot{\mathbf{R}}_{0\mathrm{a}}|$. The deceleration from $|\dot{\mathbf{R}}_{0\mathrm{a}}|$ to $|\mathbf{R}_\mathrm{a}|/\tau_\mathrm{a}$ always occurs in less then 1.25 ms, so it is at least 8 m s^{-2}. Only the pulling length $|\mathbf{R}_\mathrm{a}|$ significantly increases with the presence of sliding. Data are not sufficient to statistically confirm the independence of other parameters to sliding (power < 0.7).

From the definition of $|\mathbf{R}_\mathrm{a}|$, we obtain $\sigma_0/\alpha \sim 0.4$ mm s^{-1}. Experiments by Bullock *et al* [26] showed that the adhesion force is strongly dependent on the shear load applied by the legs. In these previous experiments, male and female beetles were immobilised, then one of their leg was pressed on the substrate and pulled proximally at a speed of 500 μm s^{-1} (so about 10 times slower than what the beetles would do in free walking). The time evolution of the shear force has been reported for a female beetle; it was measured to increase to 10.8 mN in 1.5 mm. A similar maximum friction force was observed for males in that study, though the corresponding time evolution was not reported. A pull of only 58 μm could proportionally generate a shear force of 0.42 mN, which is of the same order of magnitude as the adhesion force estimated here above from the contact area S_c. The corresponding muscular force would then be about 140 μN if only S_a is in contact, which would yield a shear stress $\sigma \sim 78$ kPa. Since the pulling speed is imposed in [26], we can infer $\alpha \sim 870$ MPa s m^{-1} and $\sigma_0 \sim 35$ kPa.

TABLE II. Claw kinematics during attachment (median values). The numbers in brackets represent quantiles 25% and 75%. Variables are defined in the main text and correspond to equations (2), (5) and (6). The p-value corresponds to a two-sample t-test on the influence of sliding. The corresponding statistical power is given in the last column (for a significance level of 0.05). Data are available in the Supplementary Material.

		Static	Sliding	t-test	
	Sample #	5	2	p	power
$t<0$	$\lvert\dot{\mathbf{R}}_{0\mathrm{a}}\rvert$ [mm s^{-1}]	$15_{[3.7,17]}$	11	0.99	0.05
	$\Psi_Y(\dot{\mathbf{R}}_{0\mathrm{a}})$	$-0.3_{[-0.5,-0.1]}$	-0.8	0.21	0.20
	$\lvert\dot{\phi}_{0\mathrm{a}}\rvert$ [rad s^{-1}]	$19_{[15,26]}$	6.3	0.19	0.20
$t>0$	$\lvert\mathbf{R}_\mathrm{a}\rvert$ [μm]	$58_{[52,76]}$	160	0.05	0.99
	$\Psi_Y(\mathbf{R}_\mathrm{a})$	$-0.9_{[-1.0,-0.8]}$	-0.7	0.21	0.69
	τ_a [ms]	$36_{[29,61]}$	52	0.59	0.07
	η	$2.6_{[2.2,2.9]}$	2.2	0.55	0.11
	S_a [$\times 10^{-3}$ mm^2]	$1.8_{[1.2,2.9]}$	2.2	0.98	0.05

2. *Detachment*

A typical detachment sequence is shown in Figure 13. The distal pad peeled in the distad direction. At the same time, a slight rotation of the claws is visible in this horizontal projection, which certainly corresponds to a more complex three-dimensional twist of the claws. Twisting and lifting were already identified as the two main scenarios of detachment of fly pads [25]. A combination of both is seen in most of our recordings of dock beetles. Pulling and shifting were also observed in a very few occurrences. As soon as the very last setae detached, the claw experienced a strong and sudden acceleration that made it move by as much as a hundred micrometers in the first millisecond (speed of about 100 mm s^{-1}). Then the claw decelerated and its motion converged to a constant velocity, close to the leg speed (~ 20 mm s^{-1}). This

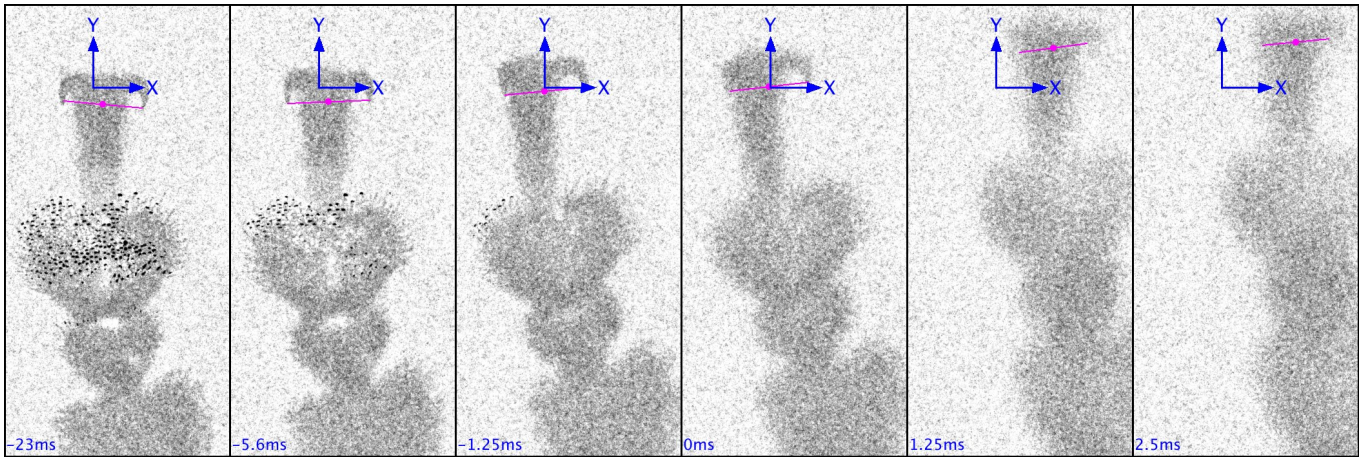

FIG. 13. Top view of the detachment of the ventral tarsus of a male right mid-leg. Time of each frame in the bottom left corner; time $t = 0$ corresponds to the last setae detaching from the substrate. Axes (X, Y) are of length 100 μm, and centred on the position of the claw at time $t = 0$. The corresponding movie is available in the Supplementary Material.

strong deceleration certainly resulted from the relaxation of some elastic structures in the tarsal chain (tarsal segments, joints) that were loaded during the stance phase, as already suggested for flies [25].

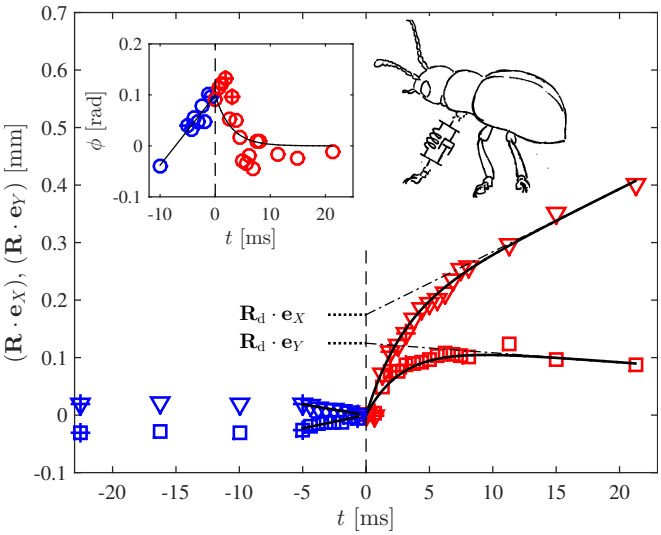

FIG. 14. Claw kinematics during detachment: Preparation (blue) and elastic recovery right after detachment (red). Triangles ($\triangledown$) represent $\mathbf{R}(t)\cdot\mathbf{e}_X$ while squares ($\square$) represent $\mathbf{R}(t)\cdot\mathbf{e}_Y$. The crossed symbols correspond to the snapshots of figure 13. The thick lines correspond to Eqs.(8–13). The horizontal dotted lines indicate the magnitude of the X and Y components of $\mathbf{R}_\mathrm{d}$ (elastic deformation of the tarsal chain). The vertical dashed line is $t = 0$. The dash-dotted lines correspond to the leg motion. The schematic illustrates the Kelvin-Voigt model of the leg and tarsal segments. (Inset) Angular position $\phi(t)$. The solid line corresponds to Eq.(8).

We quantified this motion on the 7 detachment movies (table III). During the progressive detachment of the setae ($t \in [-5, 0]$ms), the claw motion is approximated by:

$$\mathbf{R}(t) = \dot{\mathbf{R}}_{0\mathrm{d}}t \quad \phi(t) = \dot{\phi}_{0\mathrm{d}}t + \phi_{0\mathrm{d}} \tag{8}$$

The claw speed $|\dot{\mathbf{R}}_{0\mathrm{d}}|$ and angular speed $|\dot{\phi}_{0\mathrm{d}}|$ right before detachment ($t \to 0^-$) are about 3.3 mm s^{-1} and 11 rad s^{-1} respectively. This initial motion of the claw is often distad, i.e. $\Psi_Y(\dot{\mathbf{R}}_{0\mathrm{d}}) > 0$. It corresponds to a translation of about 25 μm and a rotation of 0.08 rad during the detachment time $t_d \sim 7.5$ ms (table I). There is no significant influence of sliding for $t < 0$.

We fitted the motion after detachment of the last setae ($t \geq 0$) with a Kelvin-Voigt model of the tarsal segments (spring and dashpot in parallel, as schematised in figure 14). In this model, the leg starts moving at constant velocity $\mathbf{v}_\mathrm{d}$ at some undetermined negative time. In comparison, the claw remains relatively fixed at position $\mathbf{R} \sim 0$ because of its adhesion. So the tarsal chain is progressively deformed, i.e. the spring is loaded. At time $t = 0$, when the last setae detach from the substrate, the adhesion force disappears, so the pad is suddenly submitted to the viscoelastic restoring force only. The elastic deformation of the tarsal chain at time $t = 0$ is called $\mathbf{R}_\mathrm{d}$. If the claw had followed the leg motion from the beginning, it would have been at position $\mathbf{R}_\mathrm{d} + \mathbf{v}_\mathrm{d}t$. The Newton's law for the claw and distal-most tarsal segments (beyond the spring/dashpot) is then expressed as:

$$m\ddot{\mathbf{R}} + \beta(\dot{\mathbf{R}} - \mathbf{v}_\mathrm{d}) + k(\mathbf{R} - \mathbf{R}_\mathrm{d} - \mathbf{v}_\mathrm{d}t) = 0 \tag{9}$$

where m, β and k are the effective mass, damping factor and stiffness of the tarsal chain, respectively. These latter parameters are hard to estimate, as it is still unclear which part of the leg or tarsal chain is the main contributor to compliance. Oscillations were never observed in any of the seven quantified detachment kinematics (similar to figure 14), which suggests that this mechanical system is overdamped. Moreover, since a very

strong acceleration is systematically observed at $t = 0$, the claw velocity prior detachment ($t < 0$) can be set to zero in first approximation. In other words, we assume that $|\dot{\mathbf{R}}_{0\mathrm{d}}| \ll |\mathbf{v}_\mathrm{d}|$. The solution of Eq. (9) that starts from $\mathbf{R}(0) = 0$, and $\dot{\mathbf{R}} = 0$ is:

$$\mathbf{R}(t) = \mathbf{R}_\mathrm{d} + \mathbf{v}_\mathrm{d} t + \frac{(\mathbf{v}_\mathrm{d} + \frac{\mathbf{R}_\mathrm{d}}{\tau_+})e^{-t/\tau_-} - (\mathbf{v}_\mathrm{d} + \frac{\mathbf{R}_\mathrm{d}}{\tau_-})e^{-t/\tau_+}}{\frac{1}{\tau_-} - \frac{1}{\tau_+}} \tag{10}$$

where

$$\frac{1}{\tau_\pm} = \frac{\beta}{2m}\left(1 \mp \sqrt{1 - \frac{1}{\zeta^2}}\right), \quad \zeta = \frac{\beta}{2\sqrt{km}} \tag{11}$$

Our recordings (similar to figure 14) allow for the determination of the longest timescale τ_+ that corresponds to the deceleration, but they do not have sufficient time resolution to properly estimate either the short acceleration timescale τ_- or the damping factor ζ. To assess the influence of these parameters, we define

$$F_\pm(\zeta) = \zeta^2\left(1 \mp \sqrt{1 - \frac{1}{\zeta^2}}\right) \tag{12}$$

so $\tau_\pm = \beta/(2kF_\pm)$. The function F_+ monotonically decreases from $F_+(1) = 1$ to $F_+(\infty) = 0.5$. Since $F_+(2) = 0.54$ already, we can assume in first approximation that $F_+ \simeq 0.5$ as soon as $\zeta > 2$. In this limit, $\tau_+ \simeq \beta/k$ and $\tau_- \simeq \tau_+/(4\zeta^2) \ll \tau_+$. At the deceleration timescale, the position then becomes

$$\mathbf{R}(t) \simeq \mathbf{R}_\mathrm{d}\left(1 - e^{-t/\tau_+}\right) + \mathbf{v}_\mathrm{d} t \tag{13}$$

in the limit where $|\mathbf{v}_\mathrm{d}|\tau_+ \ll 4\zeta^2|\mathbf{R}_\mathrm{d}|$.

This equation is adjusted on experimental data (parameters $\mathbf{R}_\mathrm{d}$, $\mathbf{v}_\mathrm{d}$ and τ_+), and average values of the corresponding parameters are summarised in Table III. The elastic deformation $|\mathbf{R}_\mathrm{d}|$ is of the order of 48 μm, which is comparable to the seta length. The direction of this deformation is preferentially distad on average, since $\Psi_Y(\mathbf{R}_\mathrm{d}) > 0$, and so is the initial motion of the leg. This latter is in accordance with the distad detachment peeling of the setae. Without sliding, the speed of the leg $|\mathbf{v}_\mathrm{d}|$ is about 15 mm s^{-1}, consistently with our side-view observations, and it has no preferential direction along Y. It doubles when sliding is present. Other measurements do not seem to significantly vary with sliding. The deceleration timescale τ_+ is less than 3 ms. Furthermore, right before detachment of the last setae, the adhesion force is balanced by the elastic force provided by the leg deformation. Therefore, the force exerted by the last setae is proportional to the initial acceleration of the claw:

$$\mathbf{a}_\mathrm{d} = \frac{k}{m}\mathbf{R}_\mathrm{d} + \frac{\beta}{m}\mathbf{v}_\mathrm{d} = \frac{\zeta^2}{\tau_+^2 F_+^2}\left(\mathbf{R}_\mathrm{d} + 2\tau_+ F_+ \mathbf{v}_\mathrm{d}\right) \tag{14}$$

according to equations (11-12). Since ζ is unknown, it is hard to estimate this acceleration. Nevertheless, we can infer a lower bound to $\mathbf{a}_\mathrm{d}$ by considering $\zeta = 2$. The minimum acceleration then becomes

$$\mathbf{a}_\mathrm{d} \simeq \frac{16}{\tau_+^2}\left(\mathbf{R}_\mathrm{d} + \tau_+ \mathbf{v}_\mathrm{d}\right) \tag{15}$$

Parameters of Table III yield an acceleration of at least 460 m s^{-2}, with a similar contribution from both $\mathbf{R}_\mathrm{d}$ and $\tau_+\mathbf{v}_\mathrm{d}$. It is applied to the three distal most tarsal segments, which mass is of the order of 4×10^{-8} kg. The corresponding force, about 20 μN, is indeed the same as the adhesion force expected from a small number of individual setae.

TABLE III. Detachment - claw kinematics (median values). The numbers in brackets represent quantiles 25% and 75%. Variables are defined in the main text and correspond to measurements and equations (8) and (13). The p-value corresponds to a two-sample t-test on the influence of sliding. The corresponding statistical power is given in the last column (for a significance level of 0.05). Data are available in the Supplementary Material.

		Static	Sliding	t-test	
	Sample	5	2	p	power
$t \uparrow 0^-$	$\lvert\dot{\mathbf{R}}_{0\mathrm{d}}\rvert$ [mm s^{-1}]	$3.3_{[2,5]}$	3	0.67	0.06
	$\Psi_Y(\dot{\mathbf{R}}_{0\mathrm{d}})$	$0.7_{[-0.5,0.9]}$	-0.3	0.46	0.09
	$\lvert\dot{\phi}_{0\mathrm{d}}\rvert$ [rad s^{-1}]	$11_{[4.7,27]}$	10	0.64	0.07
$t \nearrow 0$	$\lvert\mathbf{R}_\mathrm{d}\rvert$ [μm]	$48_{[33,180]}$	110	0.84	0.05
	$\Psi_Y(\mathbf{R}_\mathrm{d})$	$0.5_{[-0.2,0.7]}$	0.0	0.55	0.08
	$\lvert\mathbf{v}_\mathrm{d}\rvert$ [mm s^{-1}]	$15_{[11,20]}$	28	0.02	0.65
	$\Psi_Y(\mathbf{v}_\mathrm{d})$	$-0.1_{[-0.6,0.7]}$	0.5	0.42	0.1
	τ_+ [ms]	$2.3_{[1.1,3.1]}$	1.0	0.25	0.17

E. Correlation between claw and body motions

The synchronisation of a side view at the body scale and a top view at the pad scale allowed for the identification of correlations between the corresponding motions of the leg and the claw. Of particular interest are first the X-variables that imply some motion in the local direction X, i.e. along the posterior-anterior axis x in the body frame. They comprise the X-directional cosine $\Psi_X(\mathbf{b})$ of any vector $\mathbf{b}$, and a twist variable $\Phi_a = \dot{\phi}_{0\mathrm{a}}/|\dot{\phi}_{0\mathrm{a}}|$ (resp. $\Phi_d = \dot{\phi}_{0\mathrm{d}}/|\dot{\phi}_{0\mathrm{d}}|$) that represents the direction of claw rotation at the end of the swing phase (resp. end of the stance phase). This variable is equal to 1 if the rotation is counterclockwise (in the microscope view), and to -1 otherwise (figure 8). In order to correlate these claw variables to the leg motion in the body frame (as observed from the macroscopic side view), we define two local *leg* variables:

- $\Xi = 1$ if a right leg moves forward or if a left leg moves backwards in the body frame (i.e. swings towards negative X in the leg frame), and $\Xi = -1$

otherwise (swing in the positive X-direction, in the leg frame);

- $\chi = 1$ if a leg from the first tripod A = {FL, MR, HL} moves forward or if a leg of the second tripod B = {FR, ML, HR} moves backwards, and $\chi = -1$ otherwise.

To summarise, for attachment, we consider a set of six X-variables $\{\Xi, \chi, \Phi_\mathrm{a}, \Psi_X(\dot{\mathbf{R}}_{0\mathrm{a}}), \Psi_X(\mathbf{R}_\mathrm{a}), \Psi_X(\mathbf{v}_\mathrm{pa})\}$. The last four represent the twist direction and the X-component of the approach motion, of the pull after contact and of the peeling speed respectively. For detachment, we consider the similar set $\{\Xi, \chi, \Phi_\mathrm{d}, \Psi_X(\mathbf{v}_\mathrm{d}), \Psi_X(\mathbf{R}_\mathrm{d}), \Psi_X(\mathbf{v}_\mathrm{pd})\}$.

For each pair (i, j) of these variables, we calculated the Pearson's correlation coefficient $c_{ij} \in [-1, 1]$. We then proceeded to a principal component analysis (PCA) in order to identify subsets of correlated variables. In PCA, the correlation matrix c_{ij} is diagonalised. Each eigenvalue corresponds to the variance of the data in the direction of the associated eigenvector. We aim for the largest eigenvalue, that explains the largest part of the variance. The corresponding eigenvector then indicates the combination of variables that explains most of the observed variations. PCA results are given in table IV. Variables Ξ and χ are complementary and uncorrelated by definition, so we never consider both of them at the same time.

TABLE IV. PCA on direction variables, for attachment and detachment. The first line indicates the percentage of variance in the principal direction (i.e. the maximum eigenvalue of the correlation matrix, normalised by the number of variables). The following lines give the weight of each variable to this direction (i.e. the components of the corresponding eigenvector).

	% variance	64	63	71
Attachment	Ξ	-0.4	–	–
	χ	–	0.4	–
	Φ_a	0.5	0.5	0.5
	$\Psi_X(\dot{\mathbf{R}}_{0\mathrm{a}})$	-0.4	- 0.4	-0.4
	$\Psi_X(\mathbf{R}_\mathrm{a})$	-0.5	-0.5	-0.5
	$\Psi_X(\mathbf{v}_\mathrm{pa})\}$	-0.5	-0.4	-0.5
	% variance	50	66	62
Detachment	Ξ	-0.2	–	–
	χ	–	-0.5	–
	Φ_d	0.5	0.4	0.6
	$\Psi_X(\mathbf{v}_\mathrm{d})$	0.5	0.3	0.4
	$\Psi_X(\mathbf{R}_\mathrm{d})$	0.6	0.5	0.6
	$\Psi_X(\mathbf{v}_\mathrm{pd})$	-0.4	-0.4	-0.4

For attachment, considering either leg variable (Ξ or χ) yields the same percentage of variance (63% vs 64%) in the principal direction, which suggests that the claw motion is independent of the leg considered. Without any leg variable, 71% of the variance is in a direction where $\{\Phi_\mathrm{a}\}$ is opposed to $\{\Psi_X(\mathbf{v}_\mathrm{pa}), \Psi_X(\dot{\mathbf{R}}_{0\mathrm{a}}), \Psi_X(\mathbf{R}_\mathrm{a})\}$. It means that the approach velocity $\dot{\mathbf{R}}_{0\mathrm{a}}$, the pulling after attachment $\mathbf{R}_\mathrm{a}$, the peeling velocity $\mathbf{v}_\mathrm{pa}$ are in the negative X-direction when the approach rotation is counterclockwise ($\Phi_a > 0$) in the microscope view. A schematics of this mean trend is seen in figure 15, which also includes results on the distad/proximad direction given by $\Psi_Y(\cdot)$.

For detachment, the maximum of variance in the principal direction (66%) is obtained when the leg variable χ is included, so the detachment kinematics seems to depend on which tripod is considered. The principal direction suggests that the elastic deformation $\mathbf{R}_\mathrm{d}$ and the leg speed $\mathbf{v}_\mathrm{d}$ are opposite to the peeling velocity $\mathbf{v}_\mathrm{pd}$, and they are in the positive X-direction when the initial twist is counterclockwise ($\Phi_d > 0$). Moreover, when a leg of tripod A (resp. B) moves forward, the peeling velocity is in the direction of positive X (resp. negative X). According to figure 8, it means that mid-legs peel and detach in the same direction as their swing motion, while fore- and hind-legs detach in the direction opposite to the swing (figure 15).

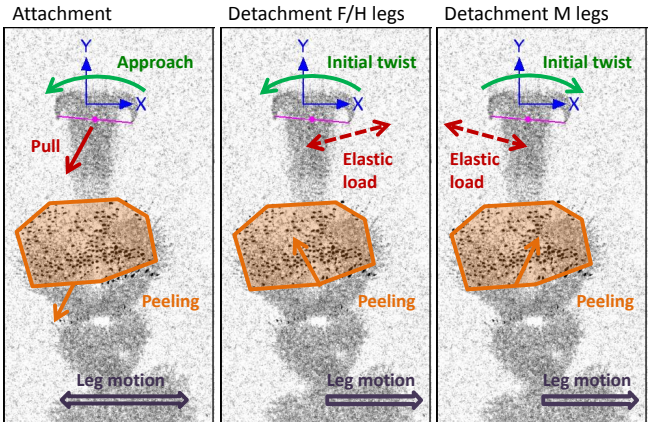

FIG. 15. Kinematic trend (top view of the ventral tarsus), based on correlations. For attachment, the scenario corresponds to any leg moving in any direction. For detachment, the scenario depends on which leg does move in which direction. Red arrows represent the proximad pull after contact during attachment $\mathbf{R}_\mathrm{a}$ and the elastic load during detachment $\mathbf{R}_\mathrm{d}$. The green arrows represent the approach before attachment ($\mathbf{R}_{0\mathrm{a}}$ and Φ_a) and the leg twist and velocity during detachment ($\mathbf{v}_\mathrm{d}$ and Φ_d). The orange arrows indicate the peeling velocities $\mathbf{v}_\mathrm{pa}$ and $\mathbf{v}_\mathrm{pd}$.

A similar PCA could be done for the magnitude of each variable (Table V). For attachment, we consider the set of variables $\{|\dot{\mathbf{R}}_{0\mathrm{a}}|, |\dot{\phi}_{0\mathrm{a}}|, |\mathbf{R}_\mathrm{a}|, \tau_\mathrm{a}, \eta, S_\mathrm{a}, |\mathbf{v}_\mathrm{pa}|, t_\mathrm{a}, S_\mathrm{c}, \varsigma\}$, where the variable $\varsigma = 1$ if the leg slides and $\varsigma = 0$ if it does not. Considering all the variables together yields only 43% of the variance in the principal direction (first eigenvector), while 23% is left to the second eigenvector. The first eigenvector is dominated by the opposition $\{|\dot{\mathbf{R}}_{0\mathrm{a}}|\}$ vs. $\{\eta, S_\mathrm{a}, |\mathbf{v}_\mathrm{pa}|, S_\mathrm{c}\}$. It indicates that slower approach (small $|\dot{\mathbf{R}}_{0\mathrm{a}}|$) and faster peeling (large $|\mathbf{v}_\mathrm{pa}|$) yield a larger contact area (η, S_a and S_c large). The second

TABLE V. PCA on direction variables, for attachment and detachment. The first line indicates the percentage of variance in the principal direction (i.e. the maximum eigenvalue of the correlation matrix, normalised by the number of variables). The following lines give the weight of each variable to this direction (i.e. the components of the corresponding eigenvector). The third and fourth columns represent the two first eigenvectors (i.e. two largest eigenvalues) associated to the full set of variables. The fifth and sixth columns represent the principal eigenvector for different subsets of variables.

	% variance	43	23	72	70
Attachment	$\lvert\dot{\mathbf{R}}_{0a}\rvert$	-0.4	-0.2	-0.4	–
	$\lvert\dot{\phi}_{0a}\rvert$	-0.1	-0.6	–	-0.5
	$\lvert\mathbf{R}_a\rvert$	-0.3	0.4	–	0.6
	τ_a	-0.2	-0.2	–	–
	η	0.4	0.2	0.4	–
	S_a	0.4	0.0	0.5	–
	$\lvert\mathbf{v}_{pa}\rvert$	0.4	0.3	0.4	–
	t_a	-0.1	-0.2	–	–
	S_c	0.4	0.0	0.4	–
	ς	-0.1	0.5	–	0.6
	% variance	30	27	63	49
Detachment	$\lvert\dot{\phi}_{0d}\rvert$	-0.2	-0.4	–	-0.4
	$\lvert\mathbf{v}_d\rvert$	0.5	-0.1	0.6	–
	$\lvert\mathbf{R}_d\rvert$	0.0	0.4	–	0.4
	τ_+	-0.4	0.1	-0.5	–
	$\lvert\mathbf{v}_{pd}\rvert$	-0.1	0.5	–	0.6
	t_d	0.4	0.0	0.3	–
	S_c	0.3	0.4	–	0.4
	ς	0.6	0.0	0.6	–
	Λ	0.1	-0.4	–	-0.4

eigenvector sheds light on another opposition $\{|\dot{\phi}_{0a}|\}$ vs. $\{|\mathbf{R}_a|, \varsigma\}$. It suggests that the rotation of the claw parallel to the substrate during the approach helps the attachment by decreasing both the likelihood of sliding and the pulling distance. These oppositions are confirmed by performing PCA on each subset of variables independently: more than 70% of the variance is then in the principal direction.

For detachment, we consider $\{|\dot{\phi}_{0d}|, |\mathbf{v}_d|, |\mathbf{R}_d|, \tau_+, |\mathbf{v}_{pd}|, t_d, S_c, \varsigma, \Lambda\}$. The latter variable $\Lambda \in [0, 1]$ indicates the possible presence of a liquid residue (figure 16), observed in about 2/3 of the movies. It represents the proportion of contact area S_c which is still covered with a liquid residue after full separation. Again, considering these nine variables together considerably spreads the variance: 30% along the first eigenvector, and 27% along the second. The first vector corresponds to the opposition $\{|\mathbf{v}_d|, t_d, \varsigma\}$ vs. $\{\tau_+\}$, which indicates that if the leg moves faster, sliding is more likely, it increases the peeling time, but after detachment the claw catches the leg faster. The second vector yields the opposition $\{|\mathbf{R}_d|, |\mathbf{v}_{pd}|, S_c\}$ vs. $\{|\dot{\phi}_{0d}|, \Lambda\}$. It suggests that a stronger attachment (high S_c) reduces the twist speed but increases the peeling speed, which then induces a larger elastic loading of the tarsal chain (high $|\mathbf{R}_d|$), and somehow results in decreased liquid footprints. This latter observation is to be compared with the previous study of Bullock *et al.* [14], which showed that both adhesion and shear stress increase with a forced depletion of the liquid. If the elastic load is somehow proportional to the shear stress, then a high load would mean that the amount of liquid in the capillary bridge is small, and so will the footprint be.

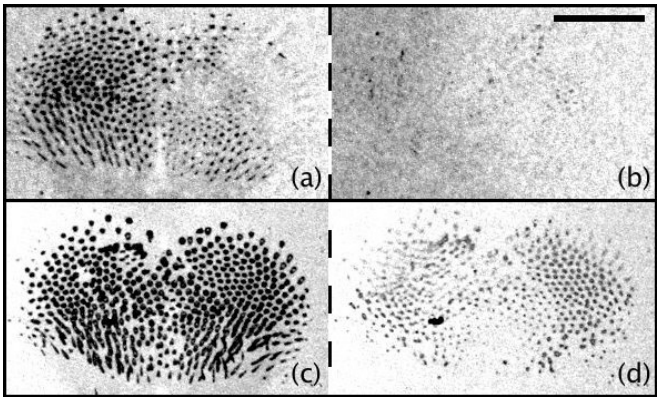

FIG. 16. (a, c) Top view of the ventral aspect of a distal pad in contact with a glass plate. (b, d) Top view of the glass plate after separation of the pad. In (b), there is no significant liquid residue. In (d), a liquid residue is left by almost every seta that was in contact in (c). The scale bar is 100 μm.

F. Kinematics of individual seta tips

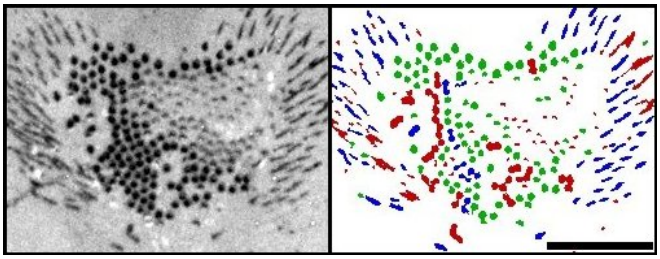

FIG. 17. Automated recognition of spatulate/discoidal (green) vs. pointed (blue) seta tips, based on shape parameters. Objects in red are discarded because their surface area is not in the appropriate range for a single fully-attached seta tip. The scale bar is 100 μm.

Finally, we measured the peeling time t_i of each individual seta tip. Similarly to t_a and t_d (figure 10), t_i is here defined as 3/2 the time required to increase the surface area of the seta tip in contact with the substrate by 2/3 of its maximum value (fully attached). We restricted these measurements to the experiments with no significant sliding. Seta tips were identified by shape recogni-

tion (figure 17). They are considered as pointed tips if the eccentricity is higher than 0.85, or as spatulate/discoidal tips otherwise. The distinction between spatulate and discoidal is almost impossible by automated image processing, owing to the limited resolution of the image. So spatulate and discoidal tips are pooled in this analysis. Their distinction will be further discussed below. For the recognition to be successful, seta tips need to be well separated from each other. The contact area of each pointed (resp. spatulate/discoidal) tip is $24_{[19,34]}\mu m^2$ (resp. $21_{[18,28]}\mu m^2$). So objects for which the maximal surface area is outside the range [15, 50] μm^2 are rejected because most likely they are either tips in partial contact or merged tips. The peeling time t_i is represented in Figure 18 for each pad, tip type and for attachment vs. detachment. The peeling time is first geometrically averaged over all the setae of a given tip shape on one video, then the statistical distribution of this average in between videos is shown as a box plot.

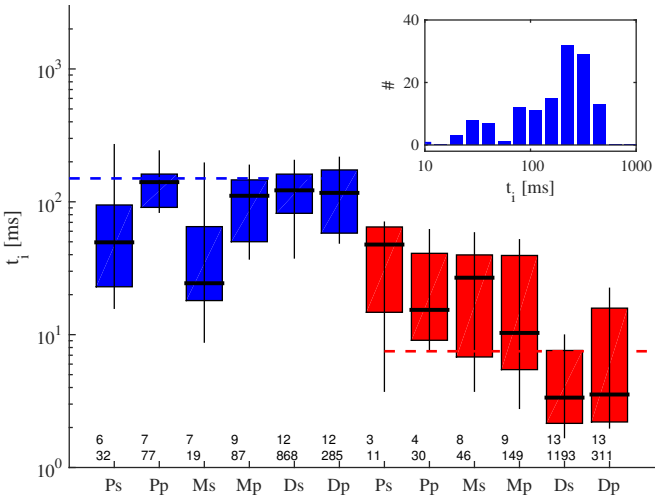

FIG. 18. Box plot of the peeling time t_i of individual seta tips. The peeling time is first geometrically averaged over setae from one video. The box and thick line then correspond to the quartiles and median of this averaged time over different videos. Whiskers correspond to quantiles 10% and 90%. The two lines of numbers refer to the sample size: the top line represents the number of videos, and the bottom line represents the total number of setae of given shape in all the videos. Attachments (resp. detachments) are represented in blue (resp. red). Pad (Proximal P, Middle M, Distal D) and tip (spatulate/discoidal s, pointed p) are indicated in abscissa. Blue and red dashed lines correspond to t_a and t_d respectively. (Inset) Histogram of t_i for spatulate/discoidal tips during the attachment of a single distal pad. Data are available in the Supplementary Material.

Again, detachment is generally about one order of magnitude faster than attachment, especially for the distal pad. The time to peel one seta tip is relatively comparable to the time required to peel the entire pads (t_a and t_d, defined in section 3 C). It suggests that the total attached surface area of the leg varies at the same pace as the area of individual seta tips. We can illustrate this further with the case of distal spatulate/discoidal setae, for which a contact length of about 5 μm is detached in about 4 ms. This yields a peeling speed of 1.25 mm s^{-1} at the tip scale, which is about 20 times less than the peeling speed of the pad $|\mathbf{v}_{pd}|$. This latter speed is calculated on the bounding box, which does not take into account the decrease in contact area of each tip (until they completely disappear). When the pad peels, the peeling front (bounding box) takes only a fraction of millisecond to travel the size of one seta tip, as already observed by Bullock *et al.* [14]. It suggests that during detachment seta tips first decrease their individual contact area (before pad peeling), and then they decrease their number (during pad peeling). The same applies to the attachment phase: the peeling speed of individual setae (5 μm in 80 ms, so about 63 μm s^{-1}) is much smaller than the peeling speed of the pad (1.1 mm s^{-1}).

Discoidal and spatulate tips were shown to have markedly different mechanical properties [17], although they are similar in diameter. In particular, discoidal tips are about 4 times stiffer than spatulate tips, and the adhesion force that they generate varies sharply with the position of the peeling line [18]. Consequently, their attachment time is expected to be smaller than the one of spatulate tips. The histogram of t_i for spatulate and discoidal tips from a single video of distal pad attachment is shown in the inset of Figure 18. Although the numbers of discoidal and spatulate tips are relatively similar on the distal pad of male dock beetles [17], the resulting distribution of peeling times does not appear bimodal. From these data, it is therefore hard to conclude about any possible difference of peeling time between spatulate and discoidal tips.

4. SUMMARY AND CONCLUSION

Our quantitative description of the walk kinematics of a dock beetle has revealed a multitude of motions at various scales: the observed phenomena span at least two orders of magnitude in time (from 2 ms to 200 ms), space (from 6 μm to 600 μm) and speed (from 60 μm s^{-1} to 30 mm s^{-1}). A synthesis of all these motions is presented in Figure 19. Our results are now summarised and discussed all together, and conclusions are drawn.

First, the free walk of a dock beetle upside-down on a smooth surface happens at a Froude number much smaller than unity. It means that at the body scale, inertial forces are negligible compared to weight and adhesion, which are therefore balancing each other at all time. We have also checked that inertia is negligible for other motions at smaller scale, except for the elastic recovery during detachment. The gait analysis revealed that the beetle may modulate its adhesion by tuning the overlap of successive swing phases. The safety factor of 9 suggests that the beetle can easily afford either partial

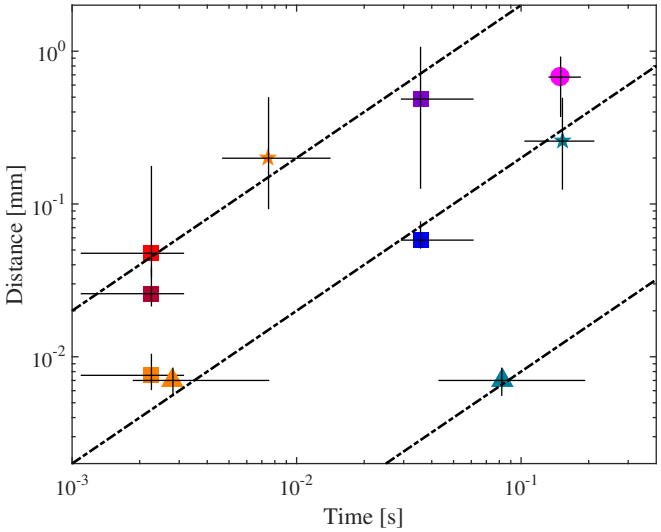

FIG. 19. Synthesis of length and time scales for each motion. (●) Leg swing, (■) approach at speed $|\dot{\mathbf{R}}_{0a}|$, (■) proximad pull at speed $|\mathbf{R}_a|/\tau_a$, (★) attachment peeling at speed $|\mathbf{v}_{pa}|$, (▲) attachment of distal spatulate setae, (▲) detachment of distal spatulate setae, (★) detachment peeling at speed $|\mathbf{v}_{pd}|$, (■) detachment preparation at speed $|\dot{\mathbf{R}}_{0d}|$, (■) viscoelastic relaxation at speed $|\mathbf{R}_d|/\tau_+$, and (■) leg speed after detachment $\mathbf{v}_d$. Error bars correspond to the interquartile range. The top dash-dotted line (resp. middle and bottom) represents a Capillary number $Ca = 0.1$ (resp. $Ca = 0.01$ and $Ca = 0.0004$).

contact or additional load.

The observed swing speed roughly corresponds to the ratio of the leg length and the hypothetical neuronal response time. It is relatively fast (20 mm s^{-1}), and so is the approach to the substrate. The leg only decelerates once in contact, through the bending and shear of the setae. The latter are sized sufficiently stiff to survive the impact; they only bend by about 1/10th of their length. A few seta tips already generate sufficient friction to strongly decelerate the leg, and a few tens of them can completely stop its motion tangential to the substrate. This deceleration is already much faster than the timescale ($\sim$ 100 ms) at which the beetle can possibly modulate the muscular force applied to its leg. Then, all the remaining setae are progressively brought into contact, usually from the most distal to the most proximal. This peeling motion is likely induced by a rotation of the pad in a vertical plane, at a timescale more comparable to the neuronal time. The pull between the first contact and complete stop is of the order of the seta length, and it is generally proximad. It may help bringing the first seta tips into intimate contact with the substrate, at the condition that these setae are initially curved distally. This seems in opposition with many SEM pictures of beetle setae available in the literature (e.g. [18, 26]), and already with the early light visualisations of Gillett *et al.* [41]. However, a closer comparison of SEM pictures (of dead beetles) and Interference Reflexion Microscopy pictures (of living beetles) in [18] clearly shows that in SEM pictures spatulate setae are curved proximally as a result of drying artefact after death. So the intrinsic curvature of hydrated setae is indeed distad, and the proximad pull favours intimate contact.

Setae are detached by peeling, both at the pad and at the seta scale. This peeling is mostly in the distad direction and it results from a three-dimensional rotation of the tarsal segments, with often a significant rotation component in the plane of the substrate (called twist here above). The claw may serve as the fulcrum of a lever, although it is not always needed. The radius of curvature at its tip is about the size of a seta tip and it is not covered with liquid, so it does not generate any significant adhesion on a smooth and rigid substrate. At every scale, detachment is surprisingly one order of magnitude faster than attachment. Our results indicate that the faster the peeling, the less liquid is left on the substrate. Detaching fast may therefore be a strategy to minimise the amount of precious liquid left as footprints on the substrate. The break-up of a liquid bridge between two parallel plates separated from each other has received significant attention, even recently [42–44]. The distribution of residual liquid between both plates is influenced by the contact angle of each when the Capillary number

$$Ca = \frac{\mu V}{\gamma} \tag{16}$$

is smaller than 0.01, where V is the characteristic speed, μ the viscosity of the adhesive liquid (here about 100 cP [45]), and γ its surface tension (here about 0.02 N m^{-1} [18]). For $Ca > 10^{-2}$ (i.e. here $V > 2$ mm s^{-1}), the liquid gets evenly distributed between the plates [46]. As seen in Figure 19, all the motions involved in detachment have a corresponding $Ca > 10^{-2}$, which suggests that they are dominated by viscous shear. This certainly helps the beetle saving its adhesive liquid even on wetting surfaces. Moreover, the detachment of seta tips involves asymmetric geometry and kinematics, by far more complicated than the normal separation of two parallel plates, and possibly in favour of minimised footprints. This amount of liquid residues on the substrate is also negatively correlated to the strength of the elastic loading of the leg before detachment, which considerably increases the speed right after detachment. Finally, the peeling speed is much larger at the pad scale than at the seta scale, which suggests that seta tips decrease their contact area before decreasing their number in contact. Since their detachment originates from the peeling rotation of the pad (which is considered as a solid body), setae are elastically loaded during this peeling, which should again increase the Ca at which liquid bridges break up. On the other hand, attachment is significantly slower and $Ca < 10^{-2}$, so the seta tips deform and come in close contact with the substrate mostly in response to surface tension loads [18].

So both attachment and detachment kinematics seem to be designed such that the adhesive liquid bridge is sub-

jected to an appropriate balance of viscous and capillary forces. Several of these motions have been similarly observed (although not quantitatively described yet) in flies [25] among others. This convergent evolution towards similar adhesive structures, tarsal kinematics in locomotion and involved attachment and detachment processes suggests that the corresponding technical solution is particularly optimal for terrestrial locomotion at the insect scale. We hope that it will therefore be a valuable source of both inspiration and design guidelines for future microrobotic pick-and-place systems based on capillary adhesion.

AUTHORS' CONTRIBUTION

SMG and TG conceived the study. SMG, SL and TG designed the experimental setup. SL and SMG carried out the experiments. TG and SMG processed the data and drafted the manuscript. PC and PL helped analysing the data and drafting the manuscript. All authors gave final approval for publication.

ACKNOWLEDGEMENTS

The authors are grateful to Y. Tourtit, A. Iazzolino, L. Tadrist and W. Federle for fruitful discussions.

DATA ACCESSIBILITY

Data extracted by image processing are accessible in an Excel file in the Supplementary Material.

COMPETING INTERESTS

We declare that we have no competing interest.

FUNDING

This work has been supported by the IAP 7/38 MicroMAST funded by BELSPO (Belgian Science Office Policy), by the FNRS research project T.0050.16 (Bioinspired passive liquid dispensing) and by a FRIA grant (FNRS, Belgium).

[1] H. F. Bohn and W. Federle, PNAS **101**, 14138 (2004).
[2] D. G. Thornham, J. M. Smith, T. Ulmar Grafe, and W. Federle, Functional Ecology **26**, 11 (2012).
[3] T. West, Trans. Linnean Soc. London **23**, 303 (1861).
[4] N. E. Stork, J. Exp. Biol. **88**, 91 (1980).
[5] E. Cheung, M. E. Karagozler, S. Park, B. Kim, and M. Sitti, in *Proceedings of the 2005 IEEE/ASME International Conference on Advanced Intelligent Mechatronics Monterey, California, USA, 24-28 July, 2005* (2005).
[6] N. J. Glassmaker, A. Jagota, C.-Y. Hui, W. L. Noderer, and M. K. Chaudhury, PNAS **104**, 10786 (2007).
[7] S. Gorb, M. Varenberg, A. Peressadko, and J. Tuma, J. R. Soc. Interface **4**, 271 (2007).
[8] L. Xue, A. Kovalev, A. Eichler-Volf, M. Steinhart, and S. N. Gorb, Nat. Comm. **6**, 6621 (2015).
[9] P. Lambert, *Capillary Forces in Microassembly*, edited by H. F. D. Liepmann, Microtechnology and MEMS (Springer, 2007).
[10] S. Uran, R. Safaric, and B. Bratina, Micromachines **8**, 182 (2017).
[11] S. Orso, U. G. K. Wegst, C. Eberl, and E. Arzt, Adv. Mater. **18**, 874 (2006).
[12] D. Voigt, N. Hosoda, J. Schuppert, and S. Gorb, Ins. Sci. **18**, 379 (2011).
[13] D. B. Zurek, S. N. Gorb, and D. Voigt, Arthr. Str. Dev. **46**, 130 (2017).
[14] J. M. R. Bullock, P. Drechsler, and W. Federle, J. Exp. Biol. **211**, 3333 (2008).
[15] S. F. Geiselhardt, S. Geiselhardt, and K. Peschke, Chemoecology **19**, 185 (2009).
[16] T. Eimüller, P. Guttmann, and S. N. Gorb, J. Exp. Biol. **211**, 1958 (2008).
[17] J. M. R. Bullock and W. Federle, Naturwissenschaften **98**, 381 (2011).
[18] S. M. Gernay, W. Federle, P. Lambert, and T. Gilet, J. R. Soc. Interface **13**, 20160371 (2016).
[19] E. Gorb and S. Gorb, Entomol. Exp. App. **130**, 222 (2009).
[20] D. Voigt, A. Schweikart, A. Fery, and S. Gorb, J. Exp. Biol. **215**, 1975 (2012).
[21] R. G. Beutel and S. N. Gorb, J. Zool. Syst. Evol. Research **39**, 177 (2001).
[22] T. Keil and R. Steinbrecht, "Insect ultrastructure," (Springer, Boston, MA, 1984) Chap. Mechanosensitive and olfactory sensilla of insects, pp. 477–516.
[23] O. Betz, Journal of Morphology **255**, 24 (2003).
[24] P. Bußhardt and S. N. Gorb, J. Exp. Biol. **216**, 319 (2013).
[25] S. Niederegger and S. N. Gorb, J. Insect Physiology **49**, 611 (2003).
[26] J. M. R. Bullock and W. Federle, J. Exp. Biol. **212**, 1876 (2009).
[27] H. Peisker, J. Michels, and S. N. Gorb, Nat. Comm. **4**, 1661 (2013).
[28] E. Wohlfart, J. O. Wolff, E. Arzt, and S. N. Gorb, J. Exp. Biol. **217**, 222 (2014).

[29] Y. Zhou, A. Robinson, U. Steiner, and W. Federle, J. R. Soc. Interface **11** (2014).
[30] G. M. Hughes, J. Exp. Biol. **29**, 267 (1952).
[31] D. M. Wilson, Annu. Rev. Entomol. **11**, 103 (1966).
[32] S. Niederegger, S. N. Gorb, and Y. Jiao, J. Comp. Physiol. A **187**, 961 (2002).
[33] S. N. Gorb, in *Handbook of adhesion technology* (Springer, 2011) pp. 1409–1436.
[34] R. T. Schuh and J. A. Slater, *True bugs of the world (Hemiptera: Heteroptera)* (Cornell University Press, 1995).
[35] C. J. Clemente and W. Federle, Proc. R. Soc. B: Biol. Sci. **275**, 1329 (2008).
[36] S. Niederegger and S. N. Gorb, J. Comp. Physiol. A **192**, 1223 (2006).
[37] L. Reinhardt, T. Weihmann, and R. Blickhan, J. Exp. Biol. **212**, 2426 (2009).
[38] S. Sponberg and R. J. Full, J. Exp. Biol. **211**, 433 (2008).
[39] R. M. Alexander and A. S. Jayes, J. Zool., Lond. **201**, 135 (1983).
[40] N. Gravish, M. Wilkinson, and K. Autumn, J.R. Soc. Interface **5**, 339 (2008).
[41] J. D. Gillett and V. B. Wigglesworth, Proc. R. Soc. B **111**, 364 (1932).
[42] J.-C. Baret and M. Brinkmann, Phys. Rev. Lett. **96**, 146106 (2006).
[43] L. Vincent, L. Duchemin, and E. Villermaux, Phys. Fluids **26**, 031701 (2014).
[44] J. Zhuang and Y. Sungtaek Ju, Langmuir **31**, 10173 (2015).
[45] B. Abou, C. Gay, B. Laurent, O. Cardoso, D. Voigt, H. Peisker, and S. N. Gorb, J. R. Soc. Interface **7**, 1745 (2010).
[46] H. Chen, T. Tang, and A. Amirfazli, Langmuir **31**, 11470 (2015).